

# A PHASE SHIFTING AND NULLING INTERFEROMETER FOR TPF

T.Velusamy , C.A Beichman, M. Shao, H. Yorke

Jet Propulsion Laboratory, California Institute of Technology,  
Pasadena, CA 91109

## ABSTRACT

We present an interferometer design that provides a null at the star and a direct measurement of both visibility amplitude and phase of the planets. The basic design is that of a two element interferometer. Each element itself is a nulling interferometer which produces a null beam formed by combining 3 telescopes of sizes (1:2:1) in a linear array on a baseline  $\sim 40$ m. They are placed on a longer baseline,  $\sim 100$ -  $1000$  m. The null beams are combined to produce a chopped output, by introducing a phase shift in one of the beams, and by switching it between  $0^\circ$  and  $180^\circ$  (cosine chop) or between  $90^\circ$  and  $270^\circ$  (sine chop). The sin/cos chops measure directly the complex visibility of the planets. Simple synthesis techniques are used for image reconstruction from the complex visibilities measured in a number of u-v points by rotating the baselines. The null width is independent of the spatial resolution, hence there is no restriction to the maximum baseline. The longer baselines possible now, help resolving out the exo-zodi. Because of its ability to measure the visibility phase this scheme shows an enhanced capability for planet detection and characterization. Milli-arcsec resolution astrophysical imaging capabilities of TPF are discussed.

Key words: Interferometry, Extra-solar Planets, Synthesis Imaging .

## 1. INTRODUCTION

The primary goal of Terrestrial Planet Finder (TPF) is direct detection of emission from extra-solar Earth-like planets and to characterize its habitable nature using infrared spectroscopy at  $7 - 20 \mu\text{m}$ . Bracewell & MacPhie (1979) first suggested

a two-element space-based infrared interferometer for planet detection, suppressing starlight by pointing a null in the interference fringe pattern on the star. Several improvements to this concept of nulling interferometry have been suggested. e.g. 4-element linear array by Angel & Wolf (1997); 2-D arrays by Leger et al 1996). Using more elements in the nulling interferometer provides greater starlight suppression. The null should be as broad (not to resolve the star) and deep as possible, at the same time not too broad to suppress the innermost planets. Also arrays with more than two elements have fringe patterns with more complex symmetry to help overcome ambiguities in the image reconstruction. Mariotti & Mannesson (1997) and Woolf et al. (1998) suggested modulating the interferometer signals (chopping) to suppress the contribution from the extended zodiacal cloud around the star. Arrays in which the individual elements themselves are nulling interferometers have been suggested by Shao (1996) and Woolf & Angel (1997) which provide both nulling and chopping. Some of these designs under investigation are described in the TPF book by Beichman et al (1999). These interferometers provide only a measure of the fringe amplitude of the planet and a cross-correlation analysis is used for image reconstruction. These images have a  $180^\circ$  ambiguity in planet's position angle (this can be removed by chopping with a phase shift as shown by Shao 1996). Simulations have shown that these configurations have limitations for planet detection when  $\text{exo-zodi} > 1Z$  (where  $1Z$  represents the solar zodiacal emission) and at inclinations  $> 30^\circ$  (Beichman & Velusamy 1997). A dual 3- element nulling interferometer has the advantage of measuring both the amplitude and phase of the visibility, providing the necessary degree of starlight suppression and exo-zodi suppression, and the required accuracy of the reconstructed images (Velusamy, Beichman & Shao 1999).

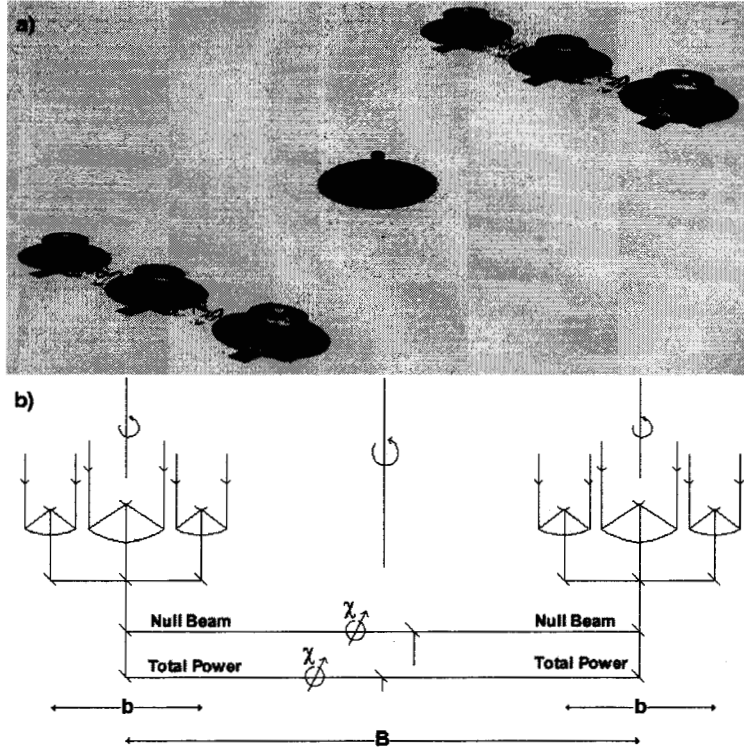


Figure 1. (a) An artist sketch of 6-telescope TPF. (b) A schematic of the nulling interferometers and the combiner for the null and total-power beams. A chopped output is obtained by switching a variable phase shift  $\chi$  in one of the null and total-power beams.

## 2. PHASE SHIFTING NULLING INTERFEROMETER

The basic design is that of a phase shifting two element interferometer. The elements themselves are nulling interferometers. Figure 1 shows schematic sketch of the 6-telescope configuration. Each element (a Mariotti nulling interferometer) produces a null beam formed by combining 3 telescopes of size (1:2:1) in a linear array. The nulling interferometer also produces a total-power beam which is useful for general astrophysical imaging. The baseline of each nulling element  $b$  is  $\sim 30$ -50m, while the separation between them is large, baseline  $B \sim 100$ -1000 m. The nulling elements can be flown on two separate free flyers and the chopper and beam combiners on a third free flyer as indicated in Figure 1a.

Because the baselines  $b$ , and  $B$  are independent, the null response characteristics (determined by  $b$ ) and spatial resolution (determined by  $B$ ) are totally de-coupled. This is a big advantage because in other configurations, increasing the baseline to achieve higher spatial resolution would lead to a narrower null which will result in less starlight sup-

pression, by resolving the central star.

A 3- telescope nulling interferometer has a null response

$$P_{null}(x,y) \sim \sin^4 \phi/2 \quad (1)$$

and a total-power response

$$P_{tp}(x,y) \sim \cos^4 \phi/2 \quad (2)$$

where  $\phi(x,y) = 2\pi b \cdot S/2\lambda$ .  $S$  is the line of sight of the off axis sky position  $(x,y)$ . The width of the null  $\sim 3$ -4 mas for  $< 10^{-6}$  at  $12\mu\text{m}$  and has an off axis null response  $\sim \theta^4$ , where  $\theta = \sqrt{x^2 + y^2}$ .

The response of a 2- element interferometer formed by the null/total-power beams with a phase shift  $\chi$  in one of the beams,

$$I_{out}(\chi) = P[1 + \cos(\Phi - \chi)] \quad (3)$$

where  $\Phi(x,y) = 2\pi B \cdot S/\lambda$ .  $P(x,y)$  is the output of the null or total-power beams of the nulling elements as given by equations 1 & 2. The response of the cosine-chop (chopped between phase shift  $\chi = 0$ , and  $\chi = \pi$ )

$$R_c(x,y) = 2P \cos \Phi \quad (4)$$

and the sine-chop (chopped between phase shift  $\chi = \pi/2$ , and  $\chi = 3\pi/4$ )

$$R_s(x, y) = 2P \sin \Phi \quad (5)$$

When  $B \gg b$ ,  $\Phi \gg \phi$ , the null/total-power response,  $P(x, y)$  as given by eq. 1 & 2 varies more slowly than the sinusoidal fringe term (in eq. 4 & 5). Thus the chopped output responses represent a sine and cosine fringe pattern as a function of  $(x, y)$  whose amplitude is modified by the slowly varying response pattern of the nulling element. Figure 2a shows the interferometer responses in the sky along the x-axis, the baseline vector  $\mathbf{B}$ . (It may be noted that when baselines  $B \sim b$ , the responses (eq. 3 & 4) are no longer sinusoidal and reduce to a complex pattern as shown for example, by Woolf & Angel (1997)). Since  $\Phi$  in eq. 4 & 5 is related to  $x, y$  in the image plane,

$$\Phi = 2\pi \mathbf{B} \cdot \mathbf{S} / \lambda = 2\pi(ux + vy) \quad (6)$$

the cos/sin chops (eq 4 & 5) measure the real and imaginary quantities of the complex visibility at the  $u-v$  corresponding to the length and orientation of baseline  $\mathbf{B}$ . Different  $u-v$  points can be sampled by rotating the baseline  $\mathbf{B}$ , while keeping the nulling baseline  $\mathbf{b}$  fixed. The image  $I(x, y)$  of the brightness around the star is obtained by Fourier transforming the complex visibilities measured at a number of  $u-v$  points.

Figure 3 shows an example of this approach for imaging a solar system analog with Mars, Venus and Earth at a distance of 10 pc. The null/total-power responses act like a primary beam in a 2-element interferometer. Figure 2b shows the effect of rotating the nulling element on the fringe pattern corresponding to a given  $u-v$  spacing. Rotating the null baseline through  $0^\circ$  to  $180^\circ$  enables that each planet is observed near the maximum in the null response at a few orientations. This allows a fairly uniform sensitivity for planet detection within the field of view, for each  $u-v$  measurement (see Figure 3). For the complex visibility at each  $u-v$  point sampled, we could use the average values measured by rotating the nulling elements. To obtain the true flux of the planets, the cleaned map is corrected for the average null response,  $\langle P_{null}(x, y) \rangle$ , as shown in Figure 3.

### 3. SIMULATIONS OF PLANET DETECTION AND CHARACTERIZATION

Direct detection of extra-solar earth-like planets requires: (i) a deep and wide null to suppress the starlight, (ii) high fidelity image reconstruction capable of detecting planet emission against a bright

exo-zodi, and its accurate flux density measurement, (iii) high enough sensitivity. The sensitivity of TPF for planet detection has been discussed by Beichman & Velusamy (1999). Planet detection alone can be relatively easy because the  $u-v$  data at all wavelengths can be combined to produce a single image. But, the characterization of the planet by its spectrum in the 7 to 20  $\mu\text{m}$  region requires a capability for accurate measurements of planet flux density at each wavelength.

The main factors that affect the fidelity of the image are the exo-zodi strength, inclination of the local ecliptic with respect to the line of sight, and structures in the exo-zodi. The  $u-v$  coverage (the number of baselines) and spatial resolution (the length of baselines) are critical factors for map fidelity. Especially the complexity of the planetary system (i.e. if several planets are present) will require a good  $u-v$  coverage. The accuracy of the planet flux measurement will also depend on the degree of uniformity of the null response across the field of view (see Fig. 3). The leakage of the star light through the null and the exo-zodi emission are the main sources of the photon noise in the outputs. The spectral study requires a uniform performance at all wavelengths. But several factors such as the null width, spatial resolution, exo-zodi flux are wavelength dependent and affect differentially the image quality and sensitivity at different wavelengths.

We made several simulations to study the merits of the imaging technique described above. We assumed a solar type star at a distance of 10 pc. The strength of the exo-zodi was varied from 1 to 10 Z. Several inclinations of the ecliptic of the extra-solar planetary systems were also studied. A randomly fluctuating component on the scale  $\sim 0.1$  AU at 0.5% level, and a 0.1 AU wide band emission with 1 AU radius at 10% level were added onto a smooth exo-zodi emission. A dual 3-element interferometer at 1 AU orbit consisting of telescopes of apertures 3.5 m and 1.75 m were assumed. The pointing jitter was 0.25 mas. An integration time of  $10^5$  sec was assumed for one set of baselines ( $b$ ,  $B$ ) and their rotation.

Figure 4 shows some examples of the images obtained by the simulations. In the case of solar system analog with 1Z, all three planets Mars, Venus and Earth are easily detected in a single wavelength map for inclinations of the ecliptic  $< 75^\circ$ ; at still higher inclinations only Earth and Venus are detectable. This result is a very significant improvement over the other configurations in which the large axial ratio in the exo-zodi for high inclinations, introduces a correspondingly large modulation in their output with rotation of the baseline.

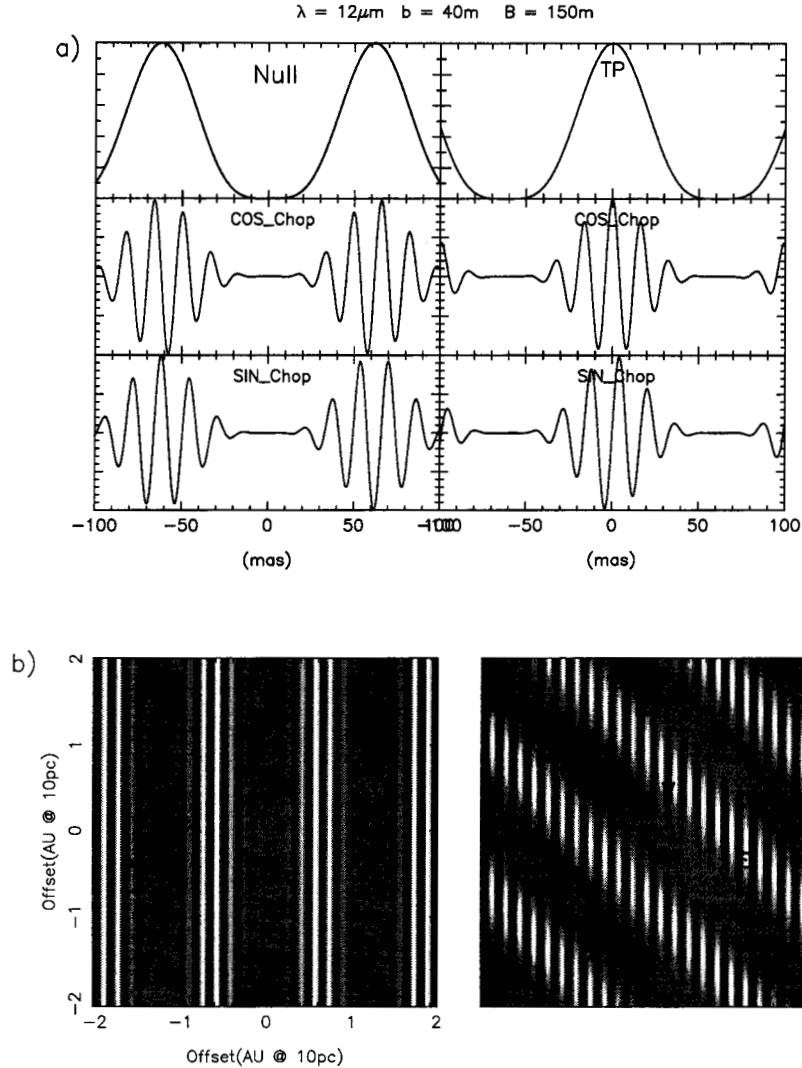


Figure 2. (a) The null/total-power and sine/cosine chop responses along the x-axis. (b) Grey scale representation of the Sine-chop fringe pattern as a function of  $(x,y)$ . The separation between the two nulling elements  $B = 150\text{m}$ , at  $0^\circ$  orientation. The nulling baseline  $b = 40\text{m}$  and orientations  $0^\circ$  (left) and  $45^\circ$  (right).

This effect is significantly reduced in the present configuration because of the sinusoidal fringe responses of the interferometer (Fig. 2) help resolving out the exo-zodi emission. Our simulations also indicate that for the 1Z cases the u-v sampling with a single baseline  $B > 100\text{m}$  is adequate to image a three planets system. This is possible because the planets are point sources and the exo-zodi is resolved out. To study the spectral capabilities of TPF, the flux densities at each wavelength were measured from the simulated maps for Earth with and without atmosphere. As shown in Figure 5, a moderate single baseline of  $\sim 150\text{m}$  provides the fidelity required to study the spectral characteristics of the planet. However, in the case of strong exo-zodi  $\sim 10\text{Z}$  longer baselines  $\geq 300\text{m}$  are re-

quired to detect Earth-like planets (see Figure 4b).

#### 4. ASTROPHYSICAL IMAGING

TPF offers a spectacular combination of high spatial resolution and sensitivity for general purpose astrophysical imaging. In principle the six-telescope configuration with appropriate beam combiners and a switch yard allows simultaneously 7 independent baselines. Even in its simplest form (Figure 1) the simultaneous interferometry of both null and total-power beams provides an excellent astrophysical imaging capabilities, especially for

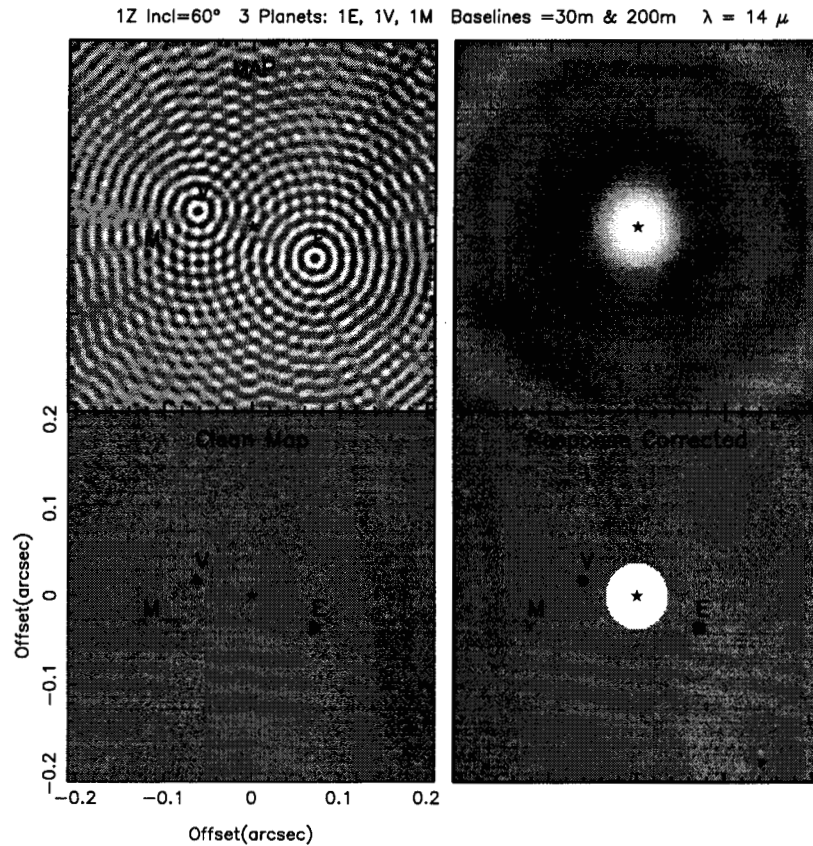


Figure 3. Imaging a solar system analog with Earth, Mars and Venus at 10 pc. The simulated complex visibilities sampled by rotating the TPF baselines were used:  $\lambda = 14 \mu$  and baselines  $b=30m$ ,  $B=150m$ . In the grey scale images the highest intensities are represented by the darkest area.

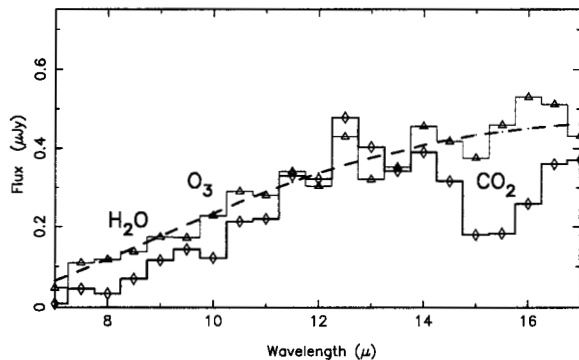


Figure 5. TPF spectrum of the Earth at 10pc. The broken line represents the black body spectrum. The points represent the flux densities observed in each wavelength in the simulated TPF images of Earth in a solar type star: ( $\diamond$ ) Earth with atmosphere and ( $\triangle$ ) without atmosphere.

the circumstellar structure of young stellar objects (YSOs). The null and total-power responses of each nulling interferometer act only as a primary

beam of a two-element interferometer (as shown in section 2). The visibilities measured by the total power beams alone would be adequate for imaging compact structures. More extended objects can be imaged by combining the visibilities of the null and the total-power beams. The main features of TPF for astrophysical imaging: Wavelength range  $\lambda \sim 3\mu m$  to  $30\mu m$ , with spectral resolution  $R \sim 20-100$ . Long baselines up to 1000m provide spatial resolution  $\sim 0.6$  mas at  $3\mu m$ ; at the distance of 150 pc (e.g. Taurus region) this corresponds to 0.1 AU ( $20 R_{\odot}$ ). It has a sensitivity of  $\Delta S \sim \text{few } \mu Jy/\text{beam}$  in 1 hr.

The milli-arcsec resolution and high sensitivity of TPF in the infrared, promises a high potential for studying some of the key YSO problems such as jet acceleration, jet collimation, accretion on to the star, all of which occur within a few AU of the star. Figure 6 shows an example of the circumstellar structure that can be probed in infrared emission by TPF. The top panels show continuum and  $H_2$  line emission at  $17 \mu m$  as derived from the accretion disk models of YSOs. The accretion models by

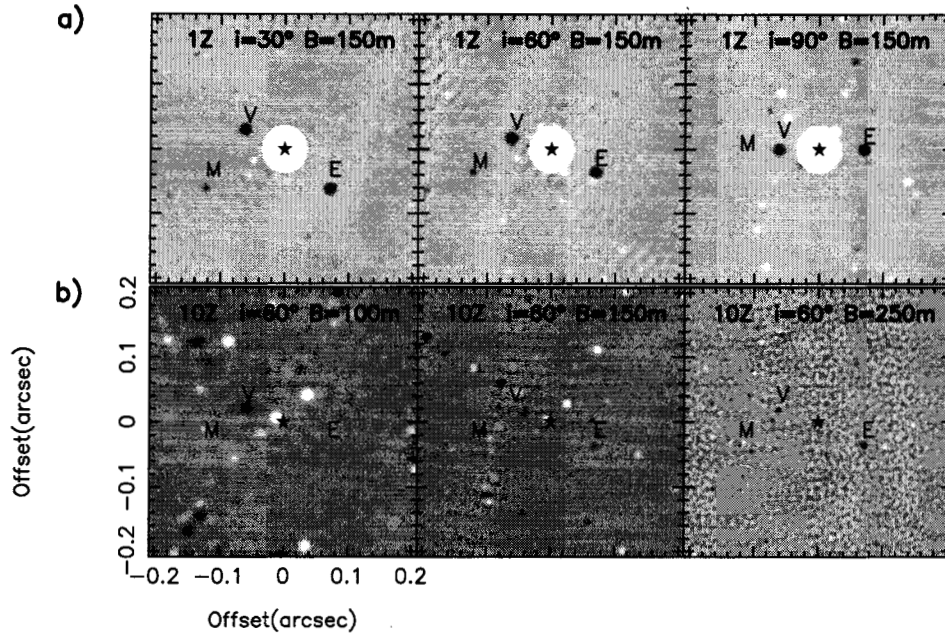


Figure 4. Imaging a solar system analog with 3 planets at  $\lambda = 14 \mu m$ . (a) Exo-zodi strength 1Z at inclinations of the ecliptic as marked. Baselines  $b=30m$ ,  $B=150m$ . (b) Effect of baseline on the image fidelity. Exo-zodi strength 10Z at inclination  $60^\circ$ . Baselines  $b=30 m$  and  $B$  as marked. Note that in stronger exo-zodi the detection of Earth requires longer baselines  $B > 300 m$ .

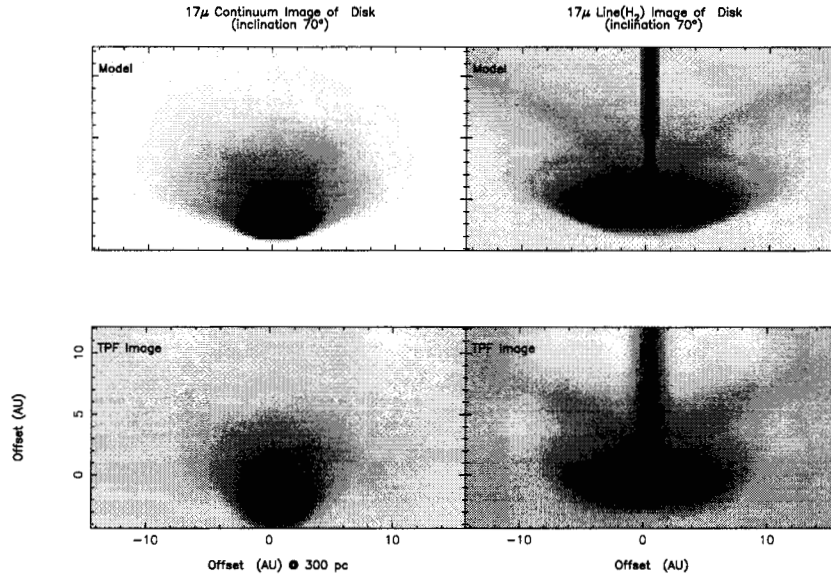


Figure 6. Simulated TPF images of accretion shocks in a YSO. Top panels are images derived from the accretion shock models for  $17 \mu m$  continuum and line emission. The lower panels are images obtained from the simulated visibilities for baselines 100 -1000m.

Yorke and Bodenheimer (1999) have been adopted to a  $1.14 M_\odot$  star with  $0.02 M_\odot$  disk. They predict the existence of an inner and an outer accretion shock on a few AU scale as material from the surrounding cloud accretes on to the disk. Using

their model temperatures and densities we derived the distribution of the infrared emission for various viewing angle with respect to the axis of the disk. A jet with constant radius and temperature ( $\dot{M} = 5 \times 10^{-7} M_\odot \text{ yr}^{-1}$ ) was also added to this bright-



ness distribution. The radiative transfer code includes the effects of scattering by dust. The jet and the shock emissions are seen more pronounced in the line emission. The lower panels in Figure 6 show the corresponding maps as imaged by TPF with 10 baselines from 100 to 1000 m. These simulations demonstrate that TPF will be able to detect and characterize disk accretion shocks and thus provide important model constraints on the process of star and disk formation.

## 5. CONCLUSION

Combined with the nulling and all the basic features of synthesis imaging, the dual 3-element interferometer offers great potential for detecting and characterizing Earth-like planets in extra-solar planetary systems. Its nulling and chopping features have several advantages over the other configurations:

1. It measures both visibility amplitude and phase.
2. It provides a straight forward synthesis imaging using the complex visibilities
3. The spatial resolution is de-coupled from the null response. There is no performance trade off between the ability to provide deep and wide null to suppress starlight and the ability for high spatial resolution. Hence there is no limit to the maximum baseline.
4. The longer baselines which are now possible enhance planet detection by resolving out the exozodi.
5. It offers a simple total-power imaging capability for general astrophysical studies.
6. This configuration may be feasible with three free flyers, while the 4- telescope OASES may require five.

## ACKNOWLEDGMENTS

Our special thanks to Shankar Velusamy and Harman Smith for the art work in Figure 1. This research was conducted at the Jet Propulsion Laboratory, California Institute of Technology, under contract with NASA.

## REFERENCES

- Angel, J.R.P., Woolf, N.J. 1997, *ApJ* 475, 373
- Beichman, C.A., Velusamy, T. in *Optical and IR Interferometry from Ground and Space*. S.C.Unwin, and R.V. Stachnick, eds. ASP Conference Series Vol.194 (San Francisco: ASP), 405
- Beichman, C.A. Woolf, N.J., Lindensmith, C.A., eds. 1999, *The Terrestrial Planet Finder*, (JPL: Pasadena, CA), JPL-99-3
- Beichman, C.A. Velusamy, T. 1997, *Bull.AAS* 29, 1310
- Bracewell, R.N., McPhie, R.H. 1979, *Icarus* 38, 136
- Leger et al. 1996, *Icarus* 123, 249
- Mariotti, J-M., Mennesson, B. 1999, internal ESA report for IRSI project
- Shao, M. 1996, in *A Road Map for the Exploration of Neighboring Planetary Systems* ("Ex-NPS report"), C.A. Beichman, ed. (JPL: Pasadena), JPL 96-22
- Velusamy, T., Beichman, C.A., Shao, M., in *Optical and IR Interferometry from Ground and Space*. S.C.Unwin, and R.V. Stachnick, eds. ASP Conference Series Vol.194 (San Francisco: ASP), 427
- Woolf, N.J., Angel, J.R.P. 1997, in *Planets beyond the solar system and the next generation of space missions*, ASP Conference Series, ed. David Soderblom, p285
- Woolf, N.J. et al. 1998, *Proc. SPIE* 3350, *Astronomical Interferometry*, R.D Reasenberg ed. 683
- Yorke, H.W., Bodenheimer, P. 1999, *ApJ* 525, 330